Hindawi Publishing Corporation
International Journal of Rotating Machinery
Volume 2013, Article ID 765142, 19 pages
http://dx.doi.org/10.1155/2013/765142

Research Article

Effects of Rotation at Different Channel Orientations on the Flow Field inside a Trailing Edge Internal Cooling Channel

Matteo Pascotto, Alessandro Armellini, Luca Casarsa, Claudio Mucignat, and Pietro Giannattasio

Dipartimento di Ingegneria Elettrica, Gestionale e Meccanica, Universita' degli Studi di Udine, via delle Scienze 208, 33100 Udine, Italy

Correspondence should be addressed to Luca Casarsa; luca.casarsa@uniud.it

Received 22 April 2013; Accepted 30 August 2013

Academic Editor: Masaru Ishizuka

The flow field inside a cooling channel for the trailing edge of gas turbine blades has been numerically investigated with the aim to highlight the effects of channel rotation and orientation. A commercial 3D RANS solver including a SST turbulence model has been used to compute the isothermal steady air flow inside both static and rotating passages. Simulations were performed at a Reynolds number equal to 20000, a rotation number (Ro) of 0, 0.23, and 0.46, and channel orientations of $\gamma = 0^\circ$, 22.5°, and 45°, extending previous results towards new engine-like working conditions. The numerical results have been carefully validated against experimental data obtained by the same authors for conditions $\gamma = 0^\circ$ and Ro = 0, 0.23. Rotation effects are shown to alter significantly the flow field inside both inlet and trailing edge regions. These effects are attenuated by an increase of the channel orientation from $\gamma = 0^\circ$ to 45°.

1. Introduction

It is a matter of fact that the adoption of proper cooling techniques is a key factor in the development of high performance and reliable gas turbine engines, since the hot gas temperature can be far above the melting point of the material used to manufacture the engine components. Focusing the attention on the internal cooling of gas turbine blades, the experimental research conducted on laboratory scaled models has played a great role in the engines development, while more recently, the availability of powerful computational tools has allowed a deeper insight into the performance of cooling channels characterized by various cross-section shapes (squared, rectangular, and triangular) and layouts (single pass, double pass).

In this regard, significant examples concerning the simulation of cooling channels for nozzle blades, in static conditions, are represented by the works of Ooi et al. [1], Lohàsz et al. [2], Luo et al. [3], Viswanathan and Tafti [4], and Spring et al. [5].

However, the recent adoption of blade profiles with a reduced thickness in the trailing edge (TE) region made the thermal protection of the TE of high pressure turbine blades one of the most challenging issues to deal with [6]. Indeed, thin blade profiles are the best choice for a high aerodynamic efficiency, but they introduce severe constraints to the cooling design. Consequently, the TE internal cooling channels have an high aspect ratio cross-section in order to be easily accommodated in the elongated profile. Jet impingement is often used to increase the heat removal, if the blade thickness allows the realization of multiple cavities as in [7]. On the other side, a single pass flow scheme best suites the thinnest blade profiles [6, 8]. Hence, the size and shape of TE ducts are quite different from those of the cooling channels at the leading edge (LE) or in the central body of the blade. Moreover, the coolant is commonly discharged in the axial direction through rectangular openings (slots) placed at the TE and through holes at the blade tip. Turbulence promoters can be used as well. In particular, elongated pin-fins named *pedestals* are often employed to ensure the mechanical strength and to enhance the heat transfer process. When the blade thickness is reduced further on, cutting material from the TE region (cut-back) can be a solution to ensure the thermal protection of thin TEs by a shield of coolant.

This solution requires even more care when designing the TE internal channel, in order to avoid unevenness of the coolant flow at the cutback that can seriously affect the aerodynamic performance of the blade. In view of these complexities, a detailed knowledge of the flow field inside the TE cooling channel is essential to understand the heat-transfer mechanisms and to guide a successful design process aimed at obtaining an effective and uniform cooling of the blade surface with pressure losses as low as possible [6].

Furthermore, if rotor blade cooling channels are considered, the effects of Coriolis and centrifugal forces on the fluid flow must be taken into account as well. The main contributions that analyse the fundamental configuration of a radial channel of rectangular cross-section in orthogonal rotation (i.e., with the rotation axis parallel to the channel height) with outward flow are the ones of Hart [9] and Speziale [10, 11]. The relative fluid flow is significantly affected by the pressure field that turns out from the effect of the Coriolis forces that act on both the peripheral and radial directions in a plane perpendicular to the rotation axis. A first consequence is the appearance of secondary flows (i.e., Coriolis vortices) which mainly act on the channel cross-section driving flow from the channel leading side to the channel trailing side at the channel mid height. Conversely, the fluid layers close to the upper and lower wall are deflected towards the channel leading side. The pressure field affects also the distribution of the radial velocity component along the channel height. As the angular velocity increases, the velocity profile shape is distorted towards a flattened distribution, resulting into a Taylor-Proudman regime at the highest rotation rates, that is, with velocity maxima found close to the walls instead of being at the channel midheight. In this regard, the rotation number, Ro, which expresses the ratio of Coriolis to inertial forces, is the parameter introduced to quantify the rotational effects.

Focusing the attention to flows in rotating cooling channels, a number of significant contributions can be found in the open literature. Reynolds averaged Navier stokes (RANS) solutions for the flow and thermal field in a rotating serpentine passage can be found in Iacovides et al. [12], while Elfert et al. [13] performed numerical predictions on a two-pass leading edge channel with ribbed walls. Unsteady RANS solutions were performed by Saha and Acharya [14, 15] in a rectangular smooth and ribbed channel to investigate the effects of the aspect ratio of the cross-section on the thermal performances. Considering more sophisticated approaches, large eddy simulations (LESs) were provided by Pallares and Davidson [16] in a rotating square channel or by Felten and Laskowski [17] in a fully developed flow through a spanwise rotating infinite serpentine passage. Direct numerical solutions (DNSs) in a same geometry can be found in [18].

Conversely, if trailing edge specific applications are considered, only a limited number of experimental or numerical contributions are available, and moreover, the majority of the works concerns ducts for nozzle blades. Taslim et al. provided two experimental and numerical contributions [19, 20] focused on the effects of jet impingement in a channel with axial outflow. A complete experimental and numerical analysis of a channel geometry similar to the one in [19] was performed by Armellini et al. [7] and Coletti et al. [21]. In these latter works, the cooling air from an adjacent passage was impinged on a rib-roughened surface at the pressure side (PS) or at the suction side (SS) wall via a series of race-track shape openings. Through particle image velocimetry (PIV) measurements, these authors obtained a deep insight into the flow, characterized by multiple primary and secondary impingements caused by the mutual arrangement of tilted crossing jets and angled ribs. Liquid crystal thermography (LCT) measurements shown the great impact of this complex flow field on the heat transfer coefficient (HTC) distribution, on both channel sides. Moreover, the detailed experimental and numerical aerothermal analysis pointed out the limits of the numerical solver in predicting the very complex flow field that develops inside the channel and hence the thermal performances. Recently, Coletti et al. [22] completed the thermal analysis on this device by means of the conjugate heat transfer measurements.

For what concerns the geometries provided with cutback, Choi et al. [23] investigated the thermal field developing in a 3-cavities channel equipped with slot and lands at the TE outlet showing the influence of Reynolds number, blowing ratio, and three different geometric configurations on static pressure, heat transfer, and film cooling effectiveness.

In the case of rotor blades channels, the only studies on cooling schemes with axial outflow, which resemble modern TE cavities, to the authors' best knowledge, are the experimental thermal analyses of Chang et al. [24], Liu et al. [25], and Rallabandi et al. [26]. In the aforementioned works, the thermal field investigations were accomplished inside a rotating channel of trapezoidal cross-section with flow ejection at the TE through holes [24] or slots [25, 26]. Even if these works provide ready-to-use correlations applicable even to models with complex geometries under rotation, it should be noted that the flow patterns hypothesized by the researches to justify the heat transfer performances still need an experimental confirmation.

The literature review allows to conclude that only a limited number of papers dealing with flow field analysis in rotating ducts relevant to turbo-machinery applications are available, especially if looking at TE solutions. Therefore, since the knowledge gained on basic geometries cannot be applied straightforward to TE cooling geometries, an effort aimed at deepening the knowledge on these devices is required.

Concerning the present cooling channel geometry, the flow field has been described by means of detailed PIV and stereo-PIV measurements in static and orthogonally rotating conditions by Armellini et al. [27]. It has been proved that the Coriolis effect alters significantly the flow field upstream of the pedestals, which results in a more uniform and axially oriented flow at the TE exit and, more importantly, with thinner boundary layers that lead to the suppression of the horseshoe vortices on the pedestal pressure side.

The present work is aimed at investigating the TE channel flow at varying the rotation number and channel orientation. The previous experimental investigations concerning a static channel and a single orthogonally rotating condition (Ro = 0.23) are extended to more realistic operating conditions by means of numerical simulations. Hence, the aim of this work

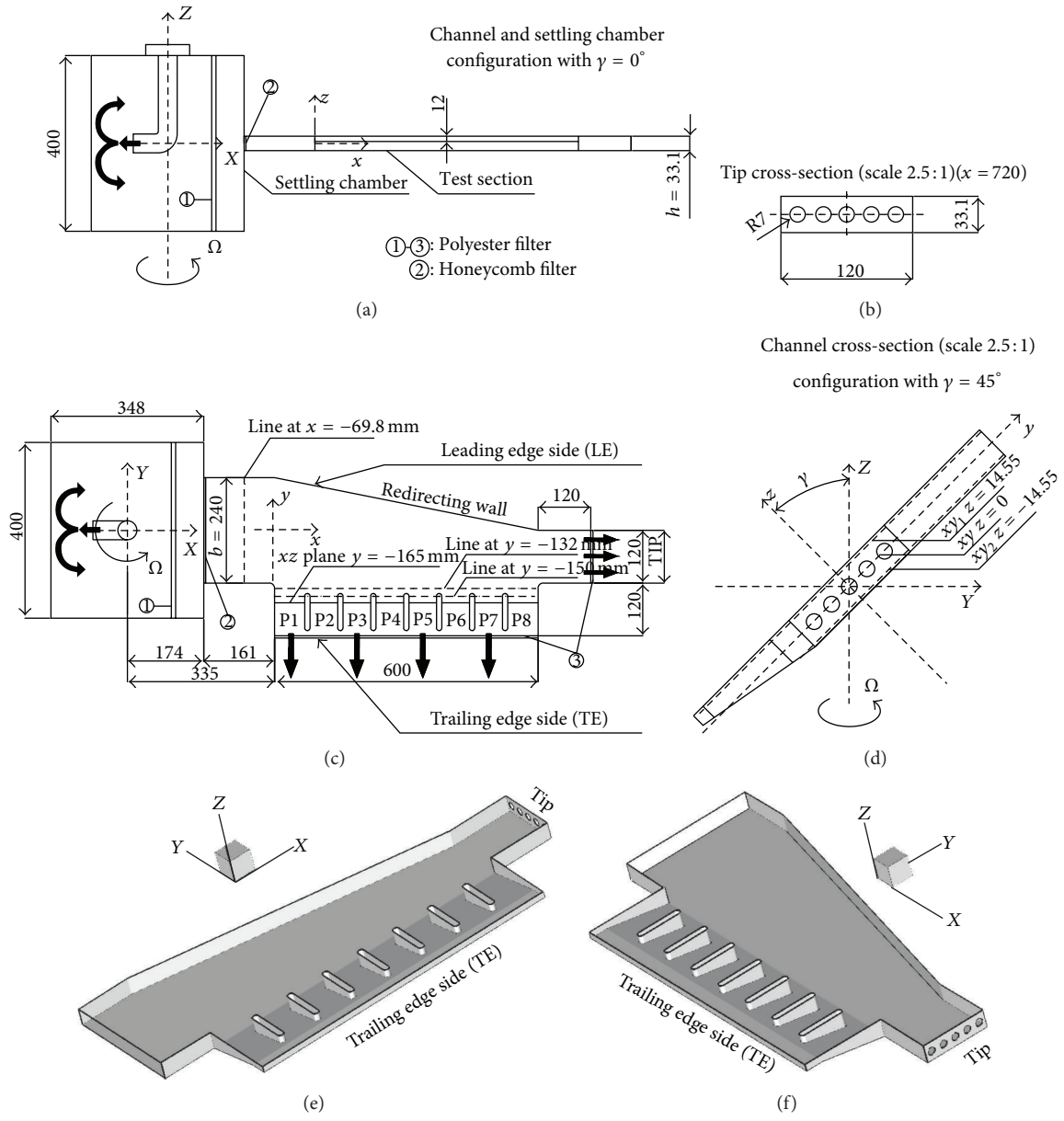

FIGURE 1: Schematic (a–d) and 3-D view (e, f) of the test section investigated in the present work, further details in [27].

is not to assess the capabilities of the numerical solver but to discuss changes in the flow field varying the angular velocity and channel orientation in order to add useful information to the few works available on this topic. In the first part of the paper, the numerical results are validated by a comparison with the experimental data available in [27]. Subsequently, the numerical results are reported for an engine-like rotation number (Ro = 0.46) and different channel orientations with respect to the rotation axis ($\gamma = 22.5^\circ$ and $\gamma = 45^\circ$).

2. Channel Geometry and Test Conditions

The investigated channel geometry has the key features of a cooling channel suitable for TE blade cooling. It has a cross-section of high aspect ratio (at the channel inlet AR = 7.25), a radial inlet, and a redirecting wall at the channel leading side that deviates the flow towards the wedge shaped outlet section at the trailing edge. Inside the TE region, seven elongated pedestals are inserted. The coolant is discharged also at the channel tip through a perforated wall. All the geometrical details and dimensions of the test section are widely commented in [27] and reported schematically in Figure 1. The channel orientation γ is defined as the angle between the axis of rotation (z-axis of the settling chamber frame of reference) and direction z normal to the channel wall (Figure 1(d)). Besides condition $\gamma = 0^\circ$ which was experimentally investigated and used for the validation of the numerical model, two more orientations are simulated, namely, $\gamma = 22.5^\circ$ and $\gamma = 45^\circ$. In fact, first stage blades of real

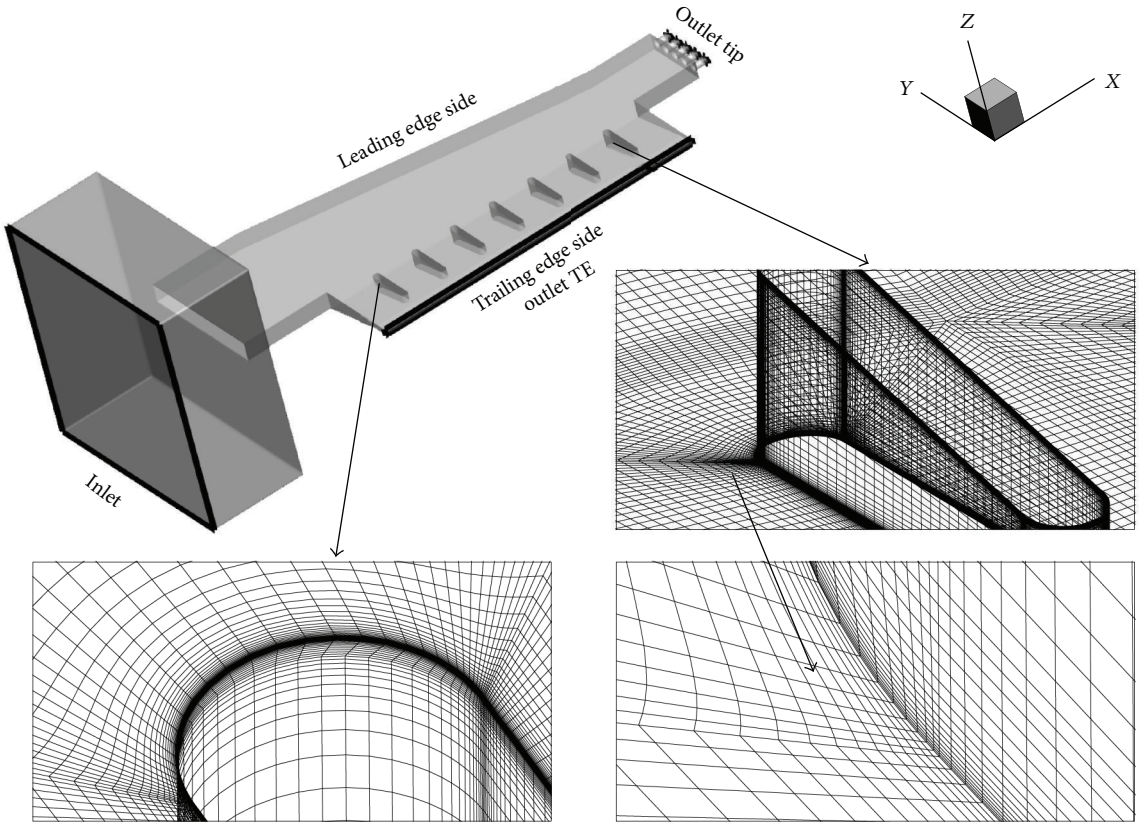

Figure 2: Overview and details of the mesh used in the present work.

engines are often highly loaded resulting in high outlet blade metal angles, that is, channel orientation angles from 20° to 45°. Finally, values Ro = 0, 0.23, and 0.46 are considered for the rotation number, while value Re = 20000 is assumed for the Reynolds number based on the bulk velocity (U_b) and the hydraulic diameter (D_h) of the channel inlet.

The experimental data used in the following for the validation of the present numerical simulations are already available in the literature [27] and have been obtained by the same authors by means of 2D and stereo-PIV measurements. The test rig allows measurements to be taken under both static and rotating conditions with the PIV image acquisition performed in phase-locked mode (i.e., the measurement chain is fixed, not rotating with the test section). A good accuracy of the data is obtained by applying a particular image preprocessing procedure as described in detail in [27, 28]. All the statistical flow quantities result from a time average computed on 1000 samples. Concerning 2D PIV data, an overall upper bound estimate of the uncertainty is less than 2% with respect to U_b (95% confidence level) in the mean velocities and 5% of U_b for the r.m.s. velocity values. According to the analysis proposed in Armellini et al. [28], the velocity uncertainty must be increased by 1% of U_b for the data acquired under rotation. Finally, referring to the stereo-PIV measurements, a crosscomparison with 2D data reported in [27] proved a satisfactory accuracy (5% U_b) also for the stereo-data.

3. Numerical Approach

Steady-state RANS numerical simulations have been performed using commercial software Ansys CFX v11.0. The convective terms were discretized by using the high resolution scheme which is a bounded second-order upwind scheme, while flow turbulence was modelled by means of the SST model with an hybrid near wall treatment [29]. The SST turbulence model has been used because it has been proved to predict reasonably well the flow field inside rotating channels [8].

Experimental data are not available for the channel orientations and rotation numbers other than the ones investigated in [27]. The lack of measured inlet velocity profiles to be used as numerical boundary conditions for $\gamma \neq 0°$ and Ro > 0.23 compelled the authors to simulate the whole channel inlet by using wider mesh that includes part of the settling chamber. An overview of the mesh is shown in Figure 2. It includes half of the inlet settling chamber and starts from a plane that contains the rotation axis. The multiblock structured mesh includes 8.04×10^6 hexahedral cells.

Such a considerable number of cells results mainly from the need of using very fine elements in the regions close to the pedestal surfaces, where three-dimensional flow separation takes place. In these regions, o-grids methodology has been used in order to obtain high cell orthogonality.

All runs have been performed by assuming an isothermal air flow. The boundary conditions were applied according to

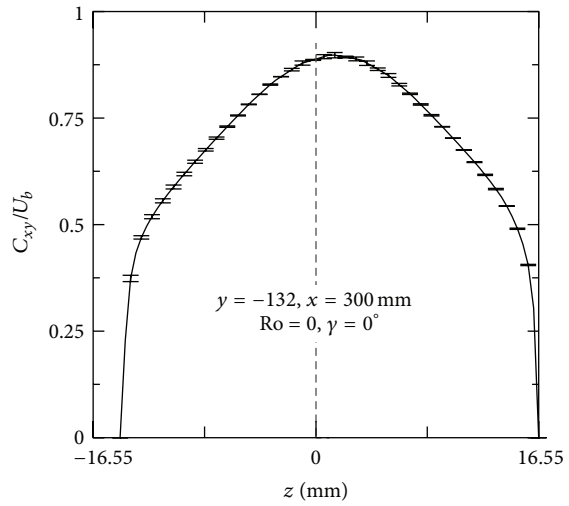

(a)

	$N \cdot 10^6$	y^+_{max}	y^+_{avg}
Coarse	1.65	2.04	0.62
Intermediate	3.64	1.53	0.45
Fine	8.04	0.98	0.33

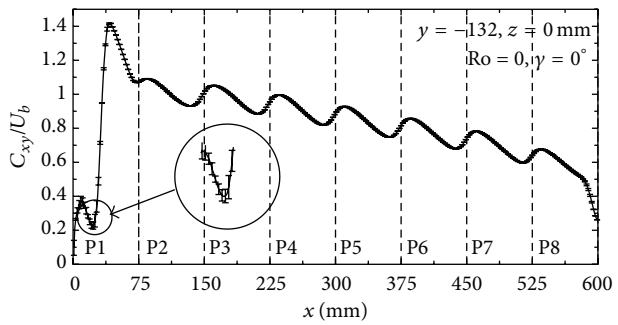

(b)

FIGURE 3: Resulting GCI error band from the mesh sensitivity analysis for the profiles of the velocity magnitude in plane xy, $C_{xy} = (U^2+V^2)^{0.5}$, extracted at $y = -132$, $x = 300$ mm (a) and $y = -132$, $z = 0$ mm (b), respectively.

a classical scheme for incompressible or low Mach number flow simulations. A uniform velocity distribution is imposed in the inlet section, while the ambient pressure (101325 Pa) is forced at the outlet.

For the assessment of numerical stability and convergence of the solution, local values of velocity components and pressure were continuously monitored during the simulations. For all the presented cases, no stability problems (i.e., significant fluctuations on the monitor quantities) were encountered and convergence was generally reached after about 200 iterations with a reduction of three to four orders of magnitude of the r.m.s. residuals.

In order to obtain an estimate of the discretization error of the computed results, a grid independence study was performed following the well-established method suggested by the Fluid Engineering Division of ASME [30]. This method has been applied to a wide range of CFD problems and it is based on a generalized formulation of the Richardson extrapolation theory [31] made by Roache [32, 33]. The method allows to compute a grid convergence index (GCI), that is, discretization error bands for the computed variables and therefore it can be regarded as standardized method to report on grid refinement studies. It is however obvious that, by its definition, the GCI method cannot account for more general modelling errors (e.g., a wrong choice of boundary conditions or turbulence model) but only for errors associated with an insufficient spatial resolution.

In the present case, the GCI method was applied to a set of three similar grids characterized by different spatial resolution defined by a refinement factor of 1.3, according to [30]. The method requires to apply the refinement factor uniformly along the three spatial directions and to use only geometrically similar cells. The main parameters and results of the mesh sensitivity analysis are provided in Figure 3, where N is the total number of cells, y^+_{max} is the maximum value of the normalized wall distance for the cells close to the walls, and y^+_{avg} is the mean value on the whole mesh.

Figures 3(a) and 3(b) show two profiles of the velocity modulus, C_{xyz}, extracted at $y = -132$ mm along z and x directions, respectively. The choice of this particular position allows the analysis to be performed over a region of the computational volume that will be widely used for the discussion of the results. Each error bar is representative of the local value of the GCI computed for the finest mesh. The analysis shows satisfactory results over all the channel height and width, with an average error below 1% with the exception

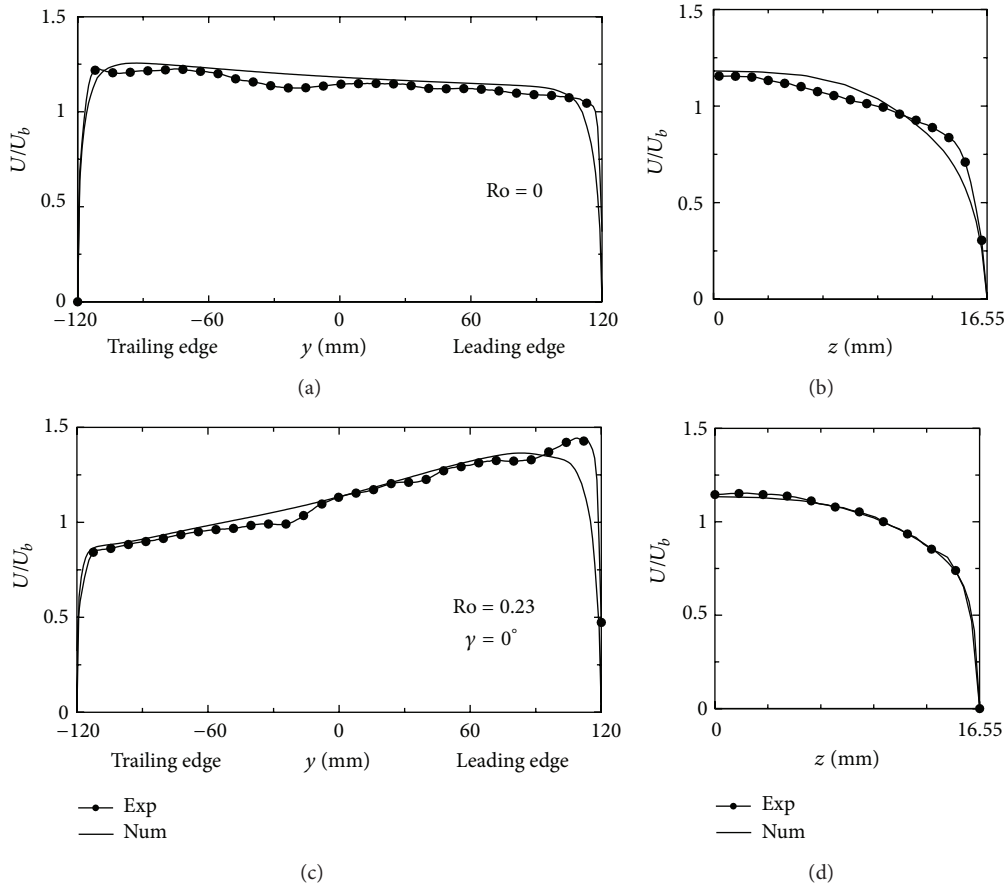

Figure 4: Experimental [27] and numerical U velocity profiles at the channel inlet, $x = -69.8$ mm.

of limited regions inside the boundary layers characterized by lower velocity and higher errors. Therefore, the finer mesh can be considered as a good compromise between spatial resolution and computational effort associated to the overall number of elements.

In the experiments that provide the validation data for the present simulations [27], a polyester fibre filter was placed at the channel exit in order to pressurize the test section, which makes the effects of the centrifugal pressure gradients negligible with respect to the ones produced by the Coriolis forces.

The filter was modelled as an isotropic porous region by introducing an additional source term in the momentum equation [29]. The kinetic pressure loss coefficient required by the solver was set to such a value that the computed pressure loss across the filter was equal to the measured one for $\gamma = 0^\circ$ and Ro = 0. The honeycomb filter (number (2) in Figure 1(a)) used in the experiments at the junction between channel and settling chamber was modelled by using the same approach, hence without requiring to mesh its specific geometry. In this case, a directional loss model was used, which required a kinetic pressure loss coefficient to be specified along both stream-wise and transverse directions. In particular, much higher losses in the transverse directions, y and z, than in the stream-wise direction, x, were forced. This results in the suppression of the transverse velocity components, V and W, as it is expected for a flow that goes through a fine honeycomb. The parameter setting was verified by comparing the velocity profiles computed at the channel inlet with the experimental data for $\gamma = 0^\circ$ and Ro = 0, 0.23.

4. Numerical Results Validation

Figure 4 shows the profiles of the mean velocity component U (nondimensionalised by the bulk flow velocity in the inlet channel, U_b) in the symmetry planes of the inlet channel at position $x = -69.8$ mm, for Re = 20000, Ro = 0, 0.23, and $\gamma = 0^\circ$.

The numerical results compare satisfactory the experimental ones, despite the limited channel length available for the flow development downstream of the honey-comb filter placed at the channel inlet ($x = -161$ mm, Figure 1(a)). The slight flow imbalance towards the TE side of the channel ($y < 0$) because of the blockage effect of the redirecting wall at the leading edge is well captured for Ro = 0 (Figure 4(a)), as well as the strong flow imbalance towards the leading edge side ($y > 0$) for Ro = 0.23 (Figure 4(c)). As previously commented in [27], the opposite flow imbalance observed in the case of rotating channel is due to potential flow effects.

In fact, the slightly viscous flow entering the channel from the settling chamber tends to conserve its angular momentum giving rise to a relative eddy whose angular velocity is opposite to the one of the rotating channel. The superposition of this counter-rotating eddy and the through-flow results in higher relative velocities in the channel leading side and lower ones in the TE region. It is interesting to note that this inviscid flow effect causes a flow imbalance that is opposite to the one expected as a consequence of the Coriolis forces. Besides the mean velocity profiles, also the predicted turbulence intensity ($I = \sqrt{2/3 \cdot \kappa}/U_b$) was checked at the same x position and $y = z = 0$, where the experimental data allow this parameter to be computed from the velocity fluctuations measured along the three spatial directions ($I = \sqrt{(u'^2 + v'^2 + w'^2)/3}/U_b$). The numerical turbulence intensity (3.9%) turns out to be comparable to the experimental value (3.28%).

The general good agreement of the numerical results with the experiments can be appreciated in the comparison of Figure 5, where time averaged in plane velocity contour plots and stream tracers in plane xy are reported. The CFD model is able to capture both the main flow features and the velocity distribution as well as their modification because of rotation. As an example, the numerical model correctly predicts a larger recirculation region at the channel tip induced by rotational effects (compare Figures 5(b) and 5(d)). However, it has to be noted that larger recirculation is always predicted in both static and rotating conditions, but this discrepancy is considered to be of minor importance in view of the scope of the present contribution. Indeed, this work is aimed at studying the effects that rotation and channel orientation have on the flow field with respect to those flow features that should have a major impact on the heat transfer performance. From this view-point, a satisfactory accuracy of the numerical predictions is achieved, indeed the numerical tool is able to capture the existence/absence of these flow features and their modifications varying the working conditions.

A more quantitative comparison between experimental and numerical data is made considering the flow approaching the pedestals. Figure 6 reports the profiles of mean flow angle α and velocity component V extracted in plane $z = 0$ at $y = -132$ mm and $y = -150$ mm, respectively. The comparison with the numerical results shows a good overall agreement for Ro = 0 (Figures 6(a) and 6(b)); more pronounced discrepancies are found in the first passage, where the CFD simulation predicts a larger flow separation with lower velocity peak and flow angle. For the other passages, the numerical results reproduce quite well the near-pedestal flow and the size of the separated flow regions. The computed flow angle for passages P5–P7 is higher then the experimental one according to the wider extension of the separated flow region at the model tip previously observed. For the case of rotating channel at Ro = 0.23 (Figures 6(c) and 6(d)) similar conclusions can be drawn, although the agreement between numerical and experimental is less satisfactory than that in the static case.

Nevertheless, the general flow structure is well captured in all cases and the complex three-dimensional interpedestal flow topology is correctly simulated for both Ro = 0 and 0.23, as shown in Figure 7 for the flow inside the interpedestal passage P4 on the xz measurement plane placed at $y = -165$ mm. For Ro = 0 (Figures 7(a) and 7(c)) both size and position of the main vortical structures are well predicted, the only significant difference being the position of the horseshoe vortex that develops on the upper side of the channel ($z > 0$). This is probably produced by the unsteady nature of this flow structure, as commented in [27]. Moreover, minor differences are put in evidence by the stream tracers path inside the recirculation bubbles ($x < 245$ mm), that can be appreciated also by the velocity components profiles in Figure 8. A justification of this is found considering a reduced measurement accuracy in that region because of the very low in-plane velocities and the lower spatial resolution when compared with the numerical one.

At this stage of the analysis, it is important to note that for Ro = 0.23, the CFD correctly predicts the disappearance of the horseshoe vortices on the upstream face of the pedestals (compare Figures 7(b) and 7(d)). As stated in [27], this can be ascribed to rotational effects that cause a significant acceleration of the near-wall flow, which leads to thinner boundary layers and hence to the disappearance of the horseshoe vortices. Indeed, the size of these secondary structures is strictly related to the boundary layer thickness. This evidence leads to conclusion that the main rotational effects are well predicted by the CFD simulations.

5. Effects of Rotation

In this section, the rotational effects are analysed on the basis of the numerical results obtained for channel configurations $\gamma = 0^\circ$ and Ro = 0, 0.23 and 0.46. For a clearer reading of the paper, it is useful to keep in mind that for $\gamma = 0^\circ$ the y-axis is aligned with the peripheral velocity.

Profiles of velocity component U in the inlet channel are shown in Figure 9 for the three rotation conditions. As Ro increases (Figure 9(a)), the flow imbalance towards the channel leading side ($y > 0$) becomes stronger, as expected in view of the dependence of the potential flow effects on the channel angular velocity [27]. In the vertical flow planes, (Figures 9(b), 9(c), and 9(d)) the shape of the velocity distributions on the channel leading side (Figure 9(d)) is almost the same, while it differentiates substantially moving towards the trailing edge (Figures 9(b) and 9(c)). In particular, for Ro = 0.46, at midchannel width position (Figure 9(c)), the U velocity profile becomes flatter with thinner boundary layers, while at the TE (Figure 9(b)) an over-speed near the confining walls is found. This behaviour is consistent with the increasing intensity of the Coriolis forces ($F_c = -2\rho\boldsymbol{\Omega} \times \mathbf{C}$, force per unit volume), which results in wider and more intense secondary structures in the channel cross-section.

This is evidenced in Figure 10 by the velocity contour plots and the time-averaged stream tracers in the channel cross-section located at $x = -69.8$ mm. As soon as the channel is rotating, the Coriolis forces produce a negative pressure gradient along the y direction; that is, higher pressures occur at the trailing side ($y < 0$). Since Coriolis forces are proportional to the velocity magnitude, inside the boundary

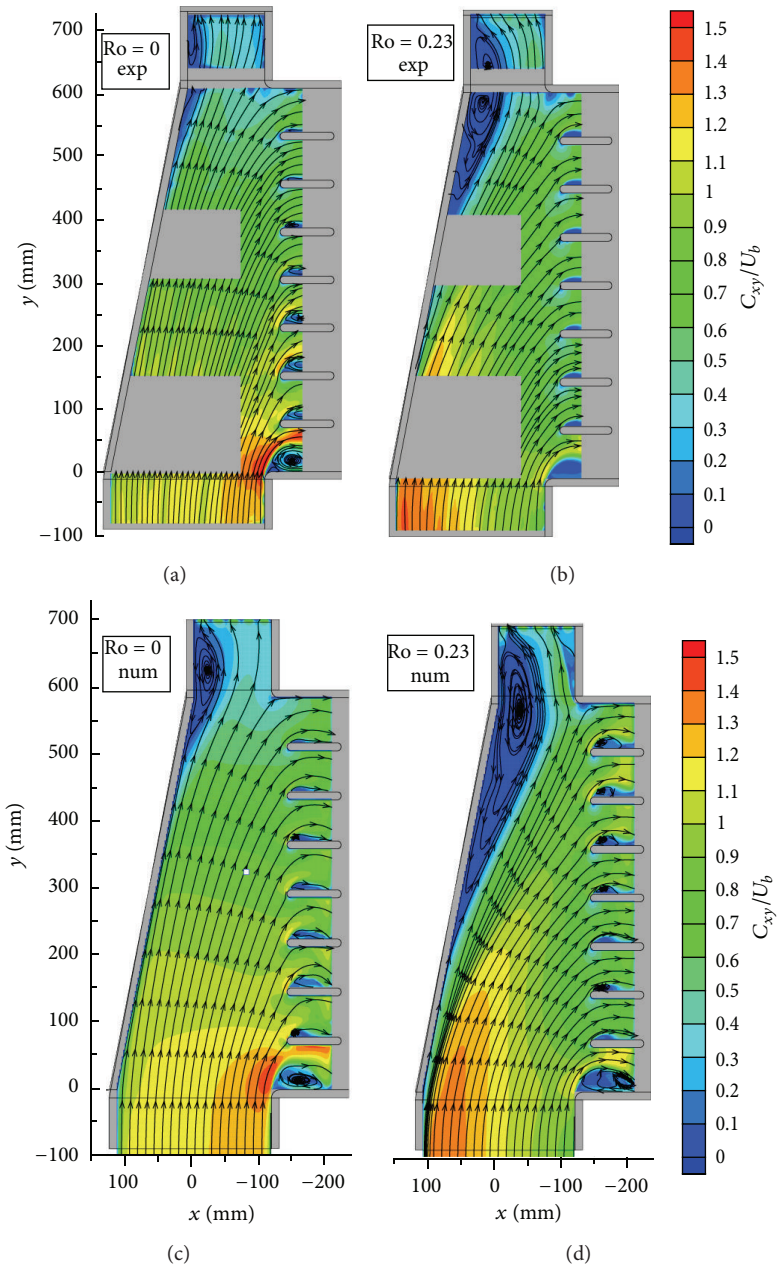

FIGURE 5: Comparison of time-averaged velocity field and stream tracers in plane xy: experimental [27] (a, b) and numerical (c, d), static (a, c), and rotating (b, d) conditions.

layers, the pressure gradient is not balanced by the local Coriolis forces, which leads to the establishment of the well-known secondary structures depicted by the stream tracers in Figures 10(b) and 10(c). When the core flow is deviated towards the trailing side ($y < 0$), the Coriolis-induced pressure gradient acquires also a stream-wise component, which is responsible for the acceleration of the boundary layer flow along the x direction. This effect is particularly evident for Ro = 0.46 at positions $y = -90$ and 0 mm (Figures 9(b) and 9(c)). Moreover, the vortices induced by rotation are confined on the channel leading side, that is, where the velocities are higher because of the potential flow effect.

The overall flow behaviour inside the channel can be commented by referring to the velocity maps and stream tracers in planes xy ($z = 0$) and xy_1 ($z = 14.55$) mm reported in Figure 11. As Ro increases, the main differences with respect to the static case are the flow accumulation near the leading side at the channel inlet and a larger separation bubble at the tip. When looking at the mean flow path on near-wall plane xy_1 ($z = 14.55$ mm, Figures 11(a), 11(b) and 11(c)), the flow deviation towards $y > 0$ imposed at the inlet by the Coriolis effect is clearly enhanced as Ro increases. Conversely, the flow in the channel central plane ($z = 0$) exhibits a deviation towards the TE side that is stronger for Ro = 0.23than for Ro = 0 and 0.46 (compare Figures 11(d),

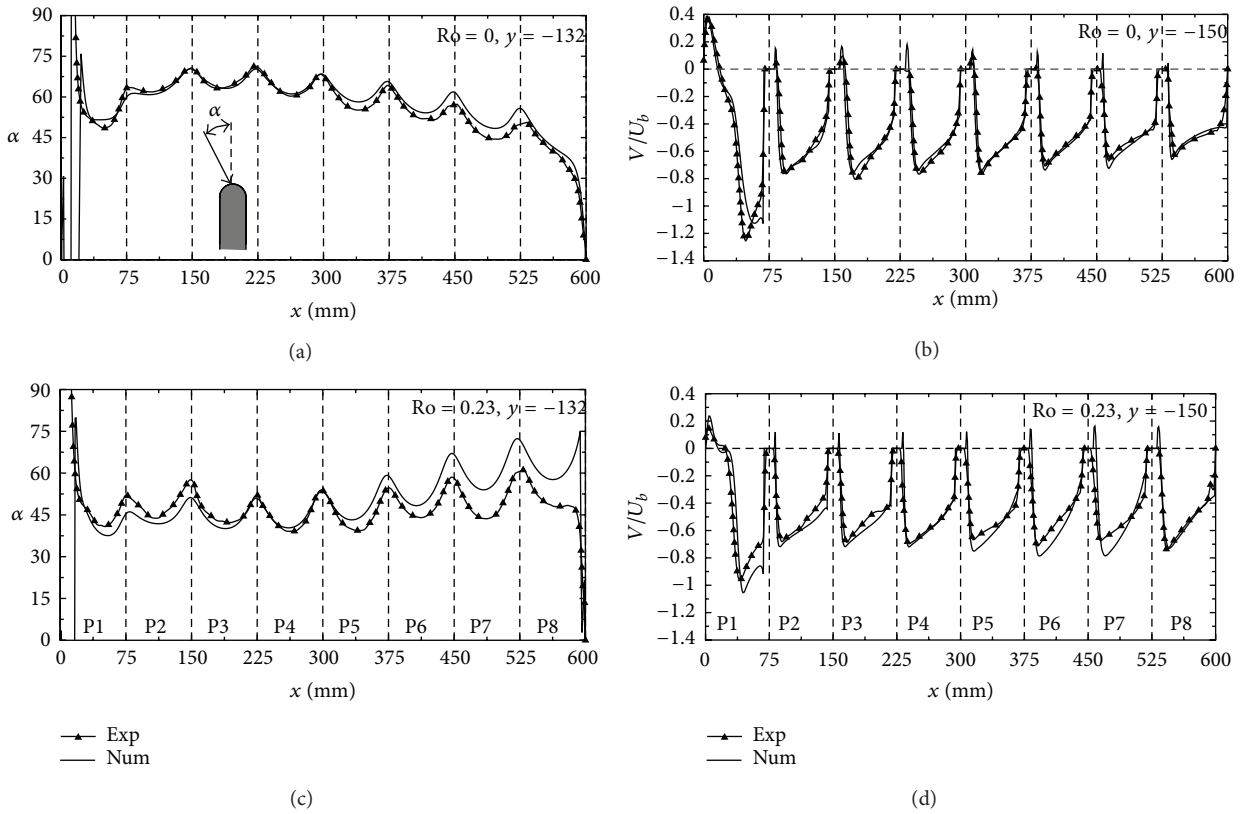

FIGURE 6: Experimental [27] and numerical flow angle profile at $y = -132$ mm, $z = 0$ mm (a, c), and V velocity profile at $y = -150$ mm and $z = 0$ mm (b, d).

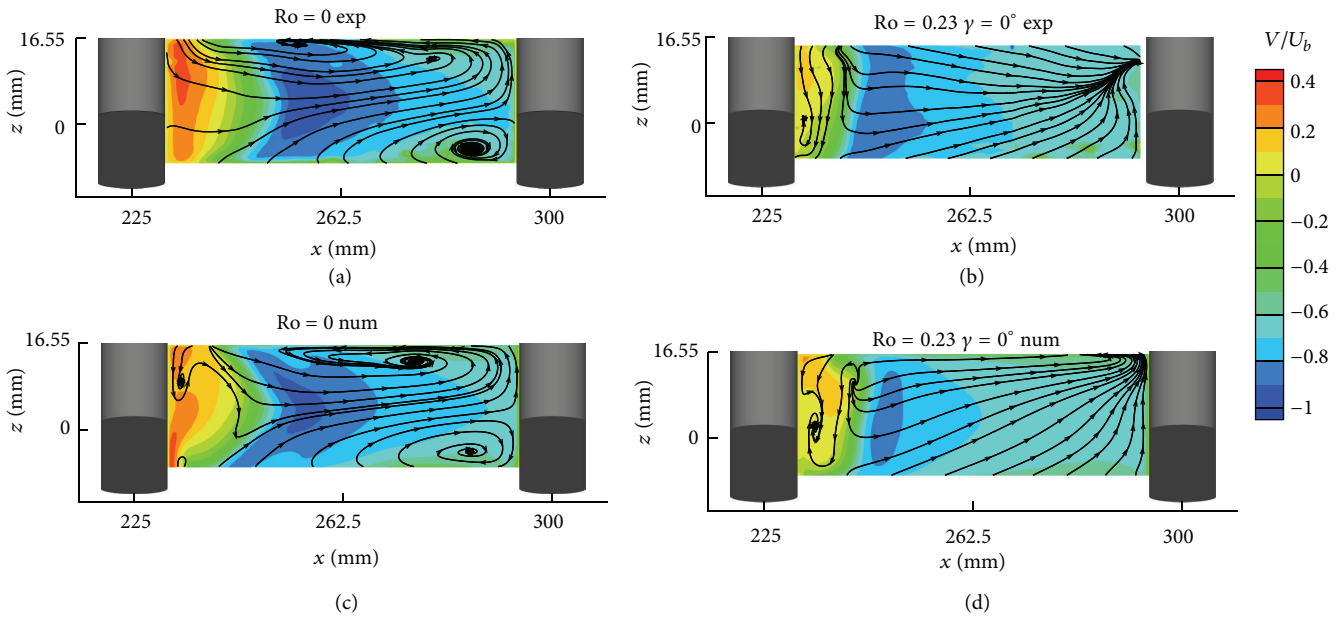

FIGURE 7: Flow field inside the interpedestal passage P4 at $y = -165$ mm for Ro = 0 (a, c) and Ro = 0.23 (b, d). Experimental [27] (a, b) and numerical (c, d) results.

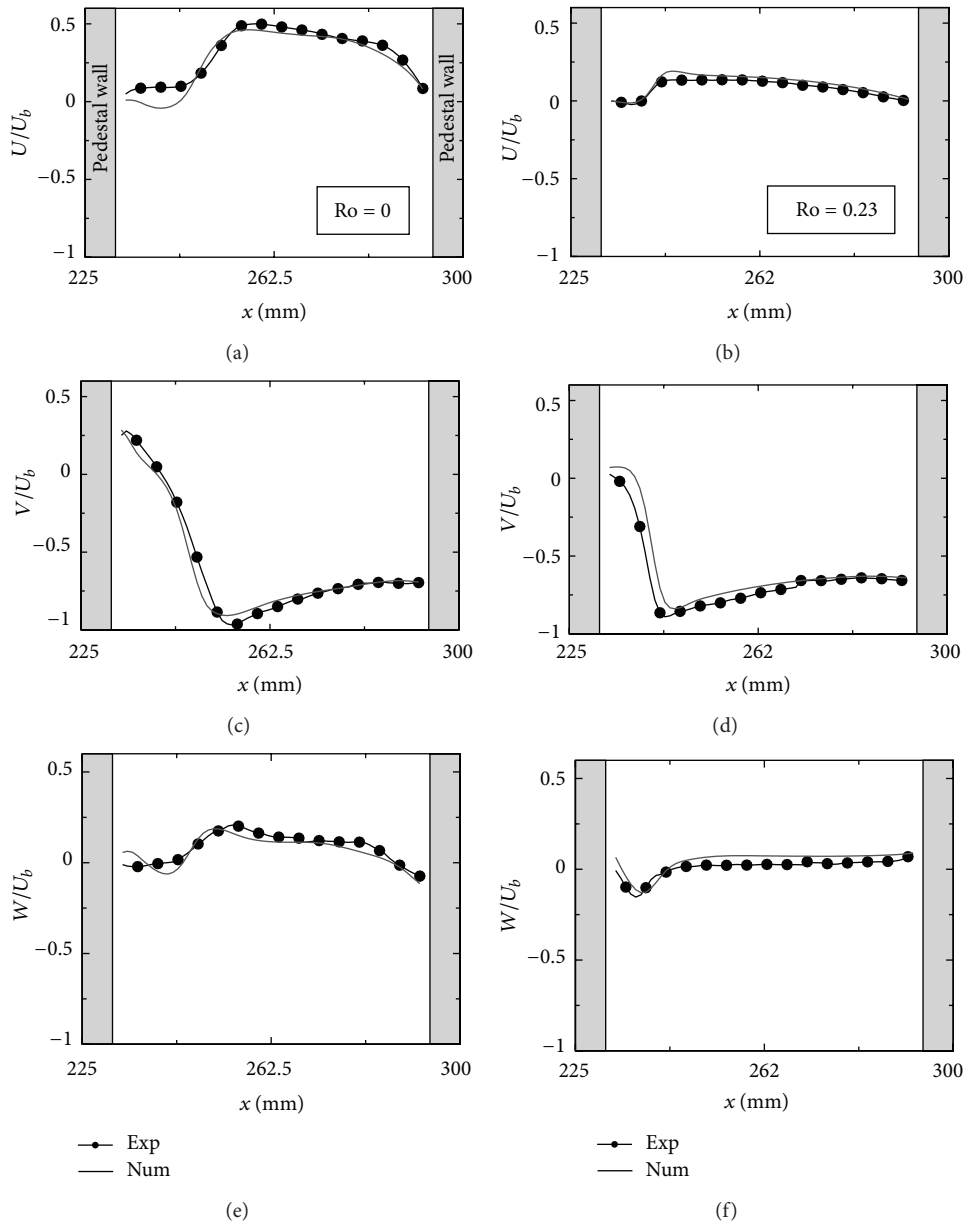

Figure 8: Comparison of experimental [27] and numerical U, V, and W velocity profiles inside the interpedestal passage P4 at $y = -165$ mm and $z = 0$ mm for Ro = 0 (a, c, e) and Ro = 0.23 (b, d, F).

11(e), and 11(f)). This trend can be explained by considering the very different velocity distributions found at the channel inlet and by taking into account the effect of the Coriolis forces in the central part of the channel where the flow is forced to deviate towards the exit slots.

To support this explanation, distributions of velocity vectors along the z-axis at different (x, y) channel positions are provided in Figure 12 and compared at varying Ro. In the static condition (Figure 12(a)), the core flow has an higher inertia than the slower flow in the boundary layers and, consistently, the former will tend to keep its radial direction while the boundary layer flow will be easily deviated towards the TE. This results in the single concavity shape of the vector distributions in Figure 12(a). A similar shape but with opposed concavity is found at Ro = 0.23 (Figure 12(b)) for most flows in the central portion of the channel. As commented above on the inlet flow, the x component of the pressure gradient induced by the Coriolis forces that act on the faster core flow causes an acceleration of the boundary layer flow along the radial direction. If Ro is increased further on (Figure 12(c)), the inlet flow distribution is completely different from that at Ro = 0 and 0.23, and it pertains to a condition of much stronger Coriolis effect. For $y < 0$, the highest flow velocities are no longer found in the core flow but close to the upper and lower walls. For the same reasons as for Ro = 0.23, the Coriolis forces will be stronger in these flow layers than in the core flow, thus causing an acceleration of this latter along the radial direction. Consequently, the

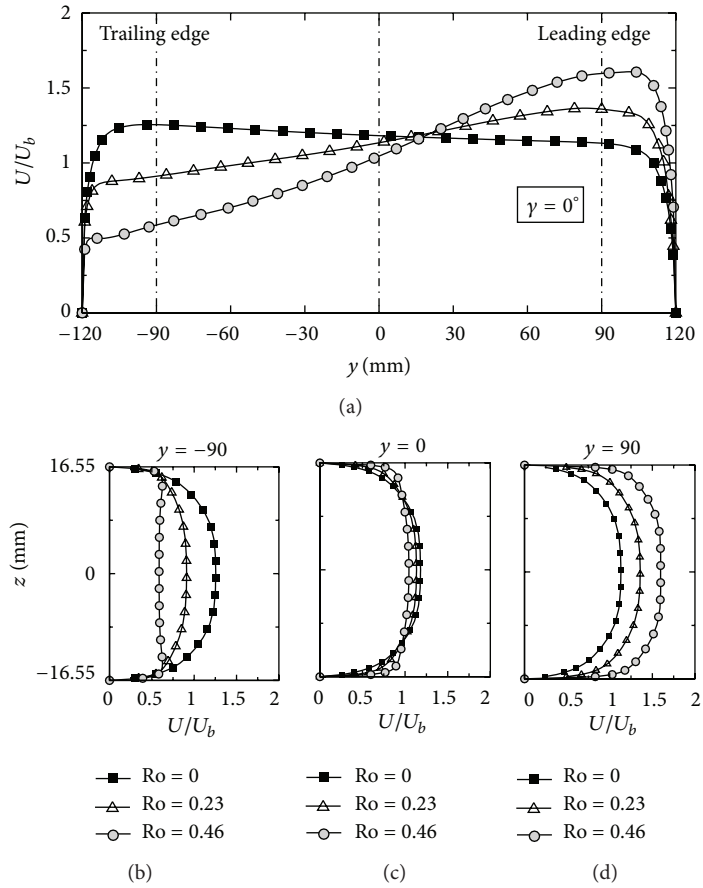

FIGURE 9: U velocity profiles at $x = -69.8$ mm for $\gamma = 0^\circ$ and different Ro. $z = 0$ mm (a), $y = -90$ mm (b), $y = 0$ mm (c), and $y = 90$ mm (d).

velocity vector distributions assume the wavy shape observed in Figure 12(c). Similar velocity distributions are found also for Ro = 0.23, but at radial positions closer to the channel tip, that is, after a sufficient space has been left for the development of the Coriolis effects.

In spite of these local effects on the flow direction, the overall effect of the channel rotation is to flatten the velocity distribution and to reduce the boundary layer thickness on the lower and upper walls. Consequently, the flow approaching the pedestal, after being deviated by the obstacle, does not produce any longer horseshoe vortices, as already commented in the previous section for Ro = 0.23. In conclusion, in the interpedestal regions. the rotational effects cause the development of a more uniform flow, characterized by a strong reduction in size of both separated flow regions and horseshoe vortices. Although this ensures a more uniform distribution of the heat transfer coefficient over the channel surfaces, the enhancement factor produced by the turbulent mixing associated with the horseshoe vortices will be lost. Concerning the mass flow splitting between the two exhaust sections of the channel, both experimental and numerical investigations show that for Ro = 0 and 0.23, about-90% of the inlet mass flow is almost uniformly discharged at the trailing edge, while the remaining 10% flows through the holes at the tip. This results from the choice of pressurizing the channel by means of filters placed at the outlet sections. In this way, the effect of the centrifugal pressure field on the overall flow structure is minimized, which points out the other rotational effects [27]. Small differences are found only for Ro = 0.46, where the numerical simulations show that about 87.5% of the inlet mass flow is discharged at the trailing edge with a linear distribution slightly increasing from 8% for P1 up to 13% for P8.

6. Effects of Channel Orientation

In this section, the numerical results obtained for different channel orientations, namely, $\gamma = 22.5^\circ$ and $\gamma = 45^\circ$, are presented.

Figure 13 shows the contour plot of velocity component U and stream tracers in the cross-section of the inlet duct at $x = -69.8$ mm and for the channel configurations $\gamma = 45^\circ$, $\gamma = 22.5^\circ$, and Ro = 0.46. These data have to be compared with those reported in Figure 10(c) for $\gamma = 0^\circ$ and Ro = 0.46. The potential flow effect is still remarkable, but the velocity distribution is no longer symmetric with respect to the channel y-axis. This results from the misalignment between the direction along which the potential effect acts (the direction of the peripheral velocity, y-axis) and the direction of the

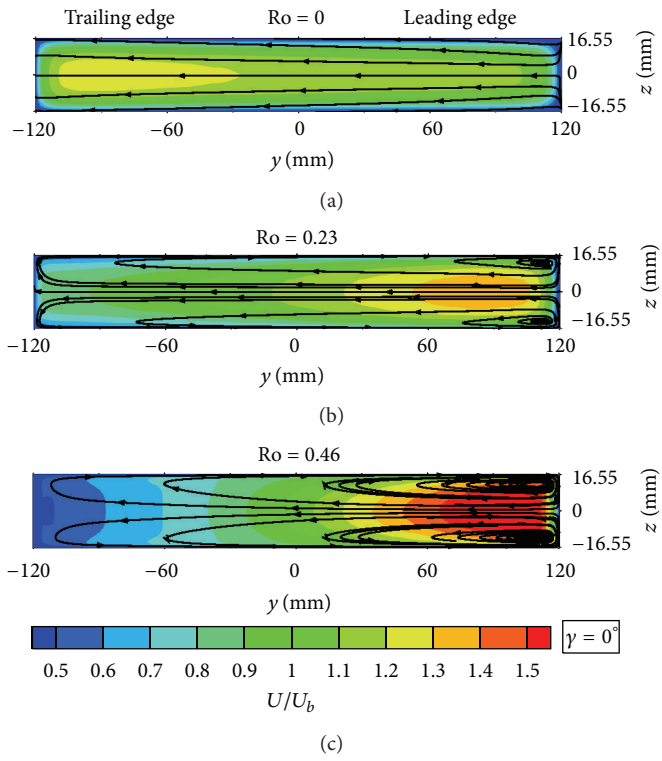

FIGURE 10: Contours of U velocity component and stream tracers at the channel inlet, $x = -69.8$ mm, Ro = 0 (a), Ro = 0.23 (b), and Ro = 0.46 (c).

channel width (y axis). For the same reason, also the Coriolis-induced vortices are not symmetric, with a larger structure detected on the lower side of the channel. The interaction of the two vortex cells in the channel corner at $z = -16.55$ mm and $y = 120$ mm causes a velocity deficit in that region, which is particularly pronounced for the $\gamma = 45^\circ$ case (Figure 13(b)).

Figure 14 shows the comparison of the inlet velocity distributions for Ro = 0.46 at varying the channel orientation. For $\gamma = 22.5,^\circ$ the velocity profiles are quite similar to those for $\gamma = 0^\circ$. On the contrary, increasing γ to 45° causes a significant reduction in the flow imbalance because of the potential effect along the channel width (Figure 14(a)). Moreover, according to the different size and position of the Coriolis-induced vortices observed in Figure 13(b), the velocity profile along the z direction at the leading side (Figure 14(d)) is modified and a flow accumulation is detected in the region $z > 0$. Finally, the reduction of the Coriolis effects on the TE side (Figure 14(b)) causes the near-wall flow accelerations observed for $\gamma = 0^\circ$ and $\gamma = 22.5^\circ$ to disappear.

Consistent with the rotational effects on the inlet flow commented above, the velocity distribution inside the main channel is not symmetric along the channel height, as shown by the velocity maps and stream tracers in Figure 15 and it is more evident for the $\gamma = 45^\circ$ case in Figures 15(d), 15(e), and 15(f). In particular, the flow deviation towards the leading side turns out to be stronger close to the lower wall of the channel than to the upper one (compare Figures 15(f) and 15(d)). The separation bubble at the channel tip is wider for $z < 0$. Indeed, the flow separation from the redirecting wall at the channel leading edge occurs further upstream at the lower elevations, as a consequence of the velocity deficit observed in Figure 13(b) at the corner of the inlet channel located at $z < 0$, $y = 120$ mm. For the intermediate configuration $\gamma = 22.5^\circ$, the effect of the channel orientation is less pronounced, but still detectable, and the flow field appears more similar to the one obtained for $\gamma = 0^\circ$.

A more quantitative comparison is performed in the plots of Figure 16. In these plots the numerical profiles of the velocity modulus C_{xyz} ($C_{xyz} = (U^2 + V^2 + W^2)^{0.5}$) are compared at different positions varying the channel orientation while Ro is kept constant. In the case Ro = 0.46 (Figures 16(d) and 16(f)), increasing γ mainly results in an asymmetric velocity distribution along the channel height, as previously commented when introducing Figure 15, and this effect is much more evident for $\gamma = 45^\circ$. However, in all cases, the velocity distributions are mostly affected by the rotational effects; that is, the highest velocities are found near the confining walls. Conversely, at lower Ro (Figures 16(a) and 16(c)), the change of the channel orientation produces major differences in the flow fields. In particular, for $\gamma = 45^\circ$, the velocity profiles at the lower radial positions (Figures 16(a) and 16(b) exhibit an almost parabolic shape associated with higher velocity peaks and thicker boundary layers, while at the larger radii (Figure 16(c)), the velocity profiles for different γ are more similar to each other. The observed differences in the flow evolution along the channel radius are associated with the effect of the channel orientation on the inlet flow. Indeed, as previously commented, at increasing γ,

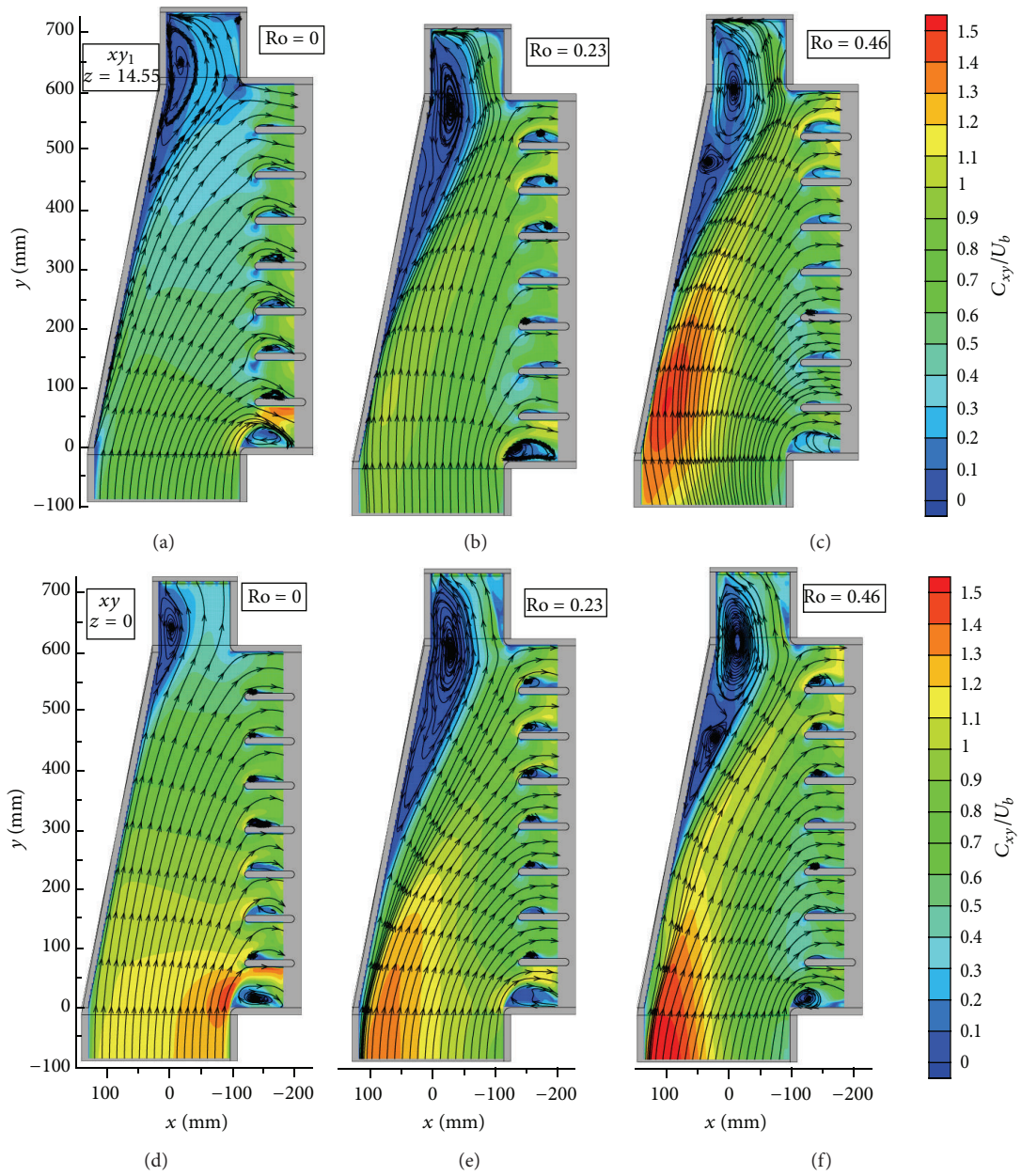

Figure 11: Contours of the in plane velocity modulus $C_{xy} = (U^2 + V^2)^{0.5}$ and stream tracers in planes xy (a–c) and xy (d–f) for Ro = 0 (a, d), Ro = 0.23 (b, e), and Ro = 0.46 (c, f). Channel configuration $\gamma = 0^\circ$.

the rotational effects at the inlet are localized near the channel leading side ($y > 0$, Figure 13) and, in consideration of the main flow path (see the stream tracers in Figures 11 and 15), they mainly influence the flow that is discharged at the larger radii of the TE. The opposite happens to the flow discharged through the interpedestal passages closer to the hub, which are fed by the inlet flow for $y < 0$.

A proof of this effect is the reappearance of the horseshoe vortices on the upstream face of the first pedestals for Ro = 0.23 and $\gamma = 45^\circ$, as shown in Figure 17. For Ro = 0.46, the rotational effects are stronger and prevail over the effect of the channel orientation. Therefore, the horseshoe vortices are not observed, as found for all the rotation numbers at $\gamma = 0^\circ$.

Finally, the mass flow through the different channel exits is not significantly affected by the variation of the channel orientation. Indeed, this depends on the fact that the pressure distribution inside the channel is only slightly affected by the different flow distributions caused by a change in the channel orientation.

7. Conclusions

In the present work, the combined effects of rotation and channel orientation on the flow field inside a modern cooling passage for the blade trailing edge were carried out through

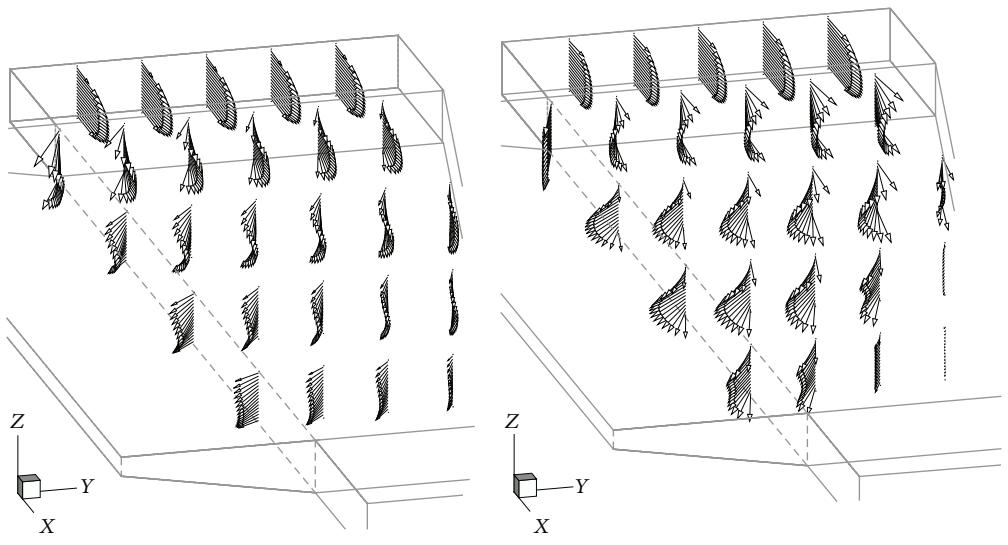

(a) Ro = 0, $\gamma = 0^{\circ}$ (b) Ro = 0.23, $\gamma = 0^{\circ}$

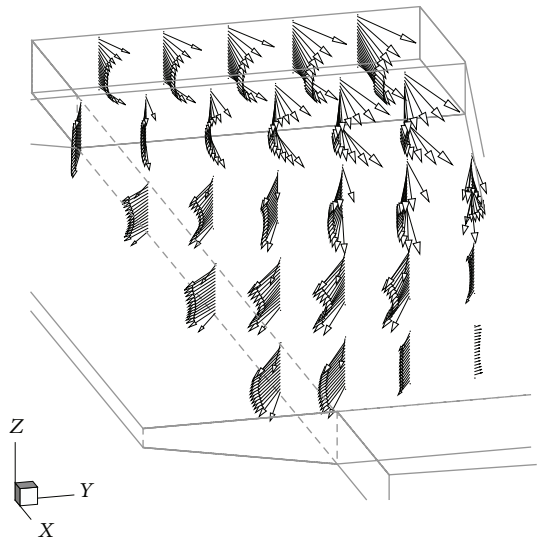

(c) Ro = 0.46, $\gamma = 0^{\circ}$

FIGURE 12: Velocity vector distributions at $x = -100$, 10, 165, 320, and 470 mm for Ro = 0 (a), Ro = 0.23 (b), and Ro = 0.46 (c). Channel configuration.

a numerical investigation performed by the SST turbulence model developed on Ansys CFX 11. The selected geometry was previously investigated by the authors in static Ro = 0 and orthogonally rotating condition, Ro = 0.23 and $\gamma = 0^{\circ}$, in order to provide a sound reference for the interpretation of the rotational effects and the database for the validation of the present computations. Coriolis forces acting on the flow field under rotation alter the pressure field inside the passage. In view of the main path of the flow, the gradient of the Coriolis-induced pressure field points towards the hub region of the TE exhaust section. This pressure gradient is not balanced by the Coriolis forces inside the slowest flow layers, which are thus accelerated in the radial direction and deflected towards the channel leading side. The outcomes of this phenomenology on the flow field for $\gamma = 0^{\circ}$ can be summarized as follows.

(i) Coriolis-induced vortical structures arise inside the inlet portion of the channel. These vortices are weak for Ro = 0.23, while they are rather stronger for Ro = 0.46. Moreover, owing to the mass flow imbalance because of the potential flow effects that act on the flow at the channel inlet, their cores are found in proximity of the leading side of the passage.

(ii) At Ro = 0.23, the velocity peak is found approximately at the channel mid-height, conversely, at Ro = 0.46 the acceleration of the near-wall flow is stronger and it is already found in the proximity of the hub.

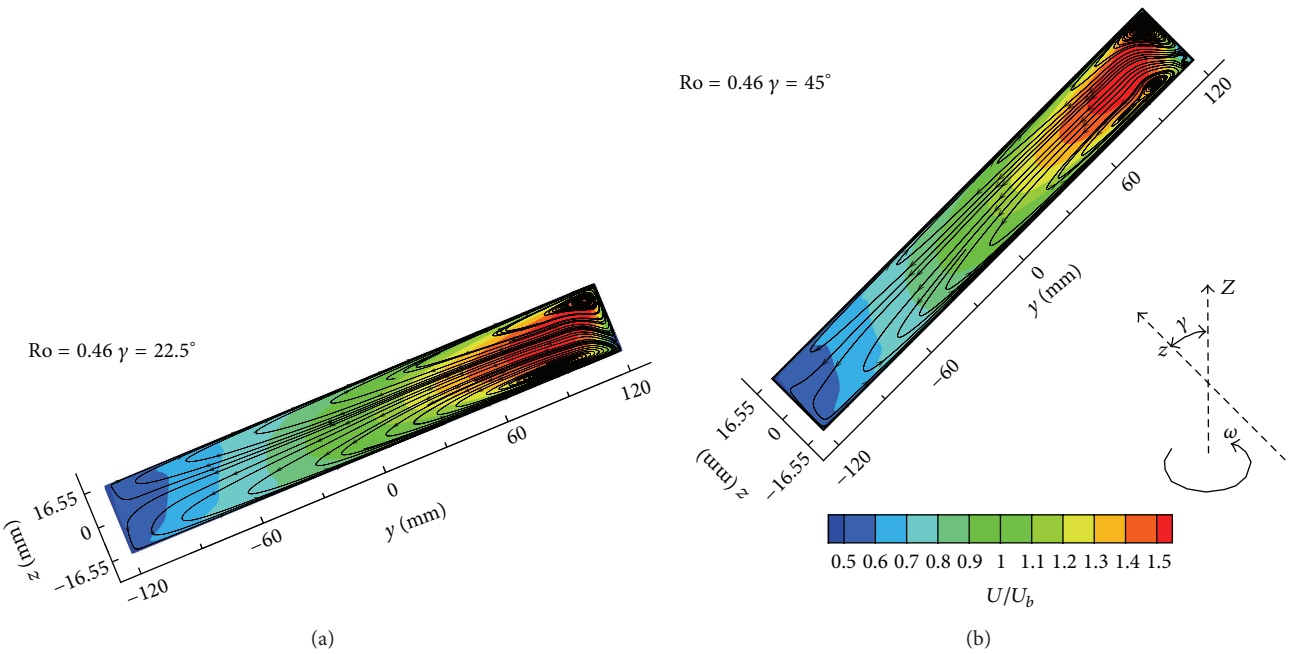

FIGURE 13: Contours of U velocity component and stream tracers at the channel inlet, $x = -69.8$ mm, for Ro = 0.46 and $\gamma = 22.5^\circ$ (a) and $\gamma = 45^\circ$ (b).

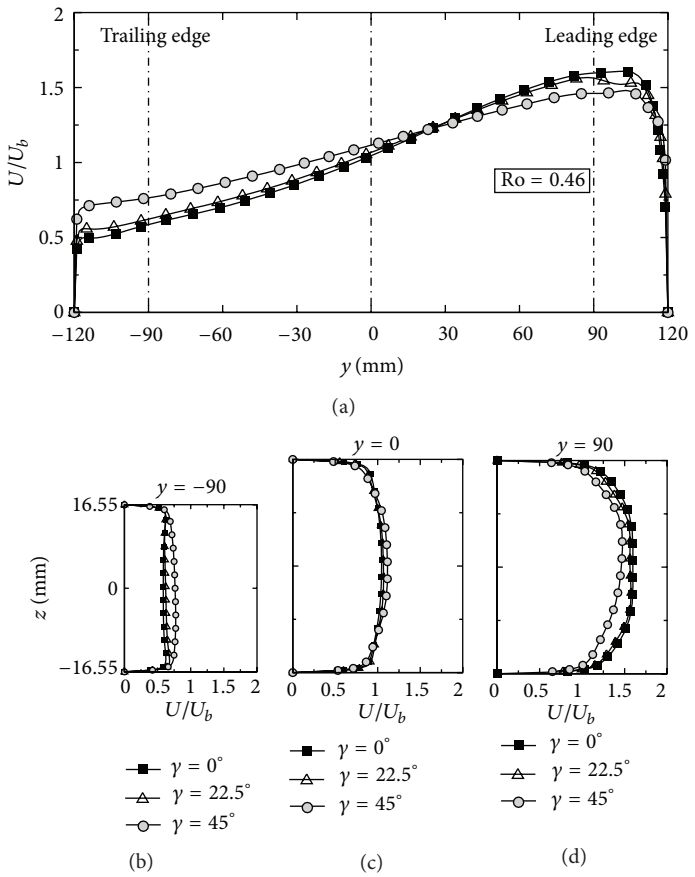

FIGURE 14: U velocity profiles at $x = -69.8$ mm for Ro = 0.46 and different channel orientations. $z = 0$ mm (a), $y = -90$ mm (b), $y = 0$ mm (c), and $y = 90$ mm (d).

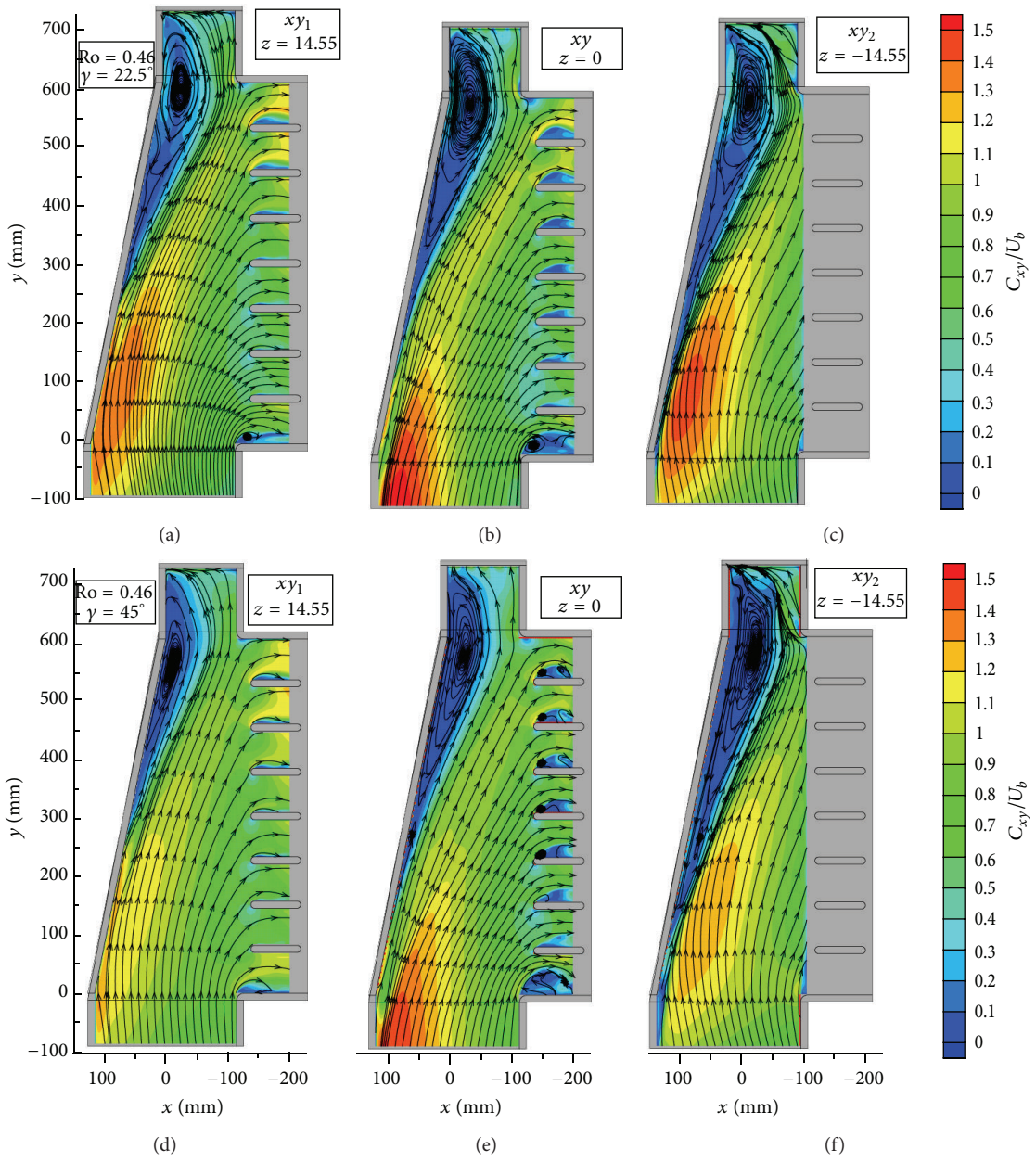

FIGURE 15: Contours of the in plane velocity modulus $C_{xy} = (U^2 + V^2)^{0.5}$ and stream tracers in planes xy_1 (a, d), xy (b, e), and xy_2 (c, f) for Ro = 0.46, $\gamma = 22.5^\circ$ (a–c), and $\gamma = 45^\circ$ (d–f).

Indeed, at Ro = 0.46 the highest velocities are found just outside the boundary layer and not at the channel mid height. The increase of Ro results in a more uniform velocity distribution along the channel height, with a strong reduction of the boundary layer thickness at both upper and bottom walls and a different swirl of the velocity vectors. The outcome of this effect on the flow field inside the exhaust region at the TE is the disappearance of the horseshoe vortices on the pedestals upstream face.

(iii) As Ro increases, the separation bubble found at the channel tip increases progressively.

When the channel orientation is different from $\gamma = 0^\circ$, a misalignment of the planes on which the Coriolis forces act with respect to the ones that contain the width of the duct (y direction) is found. Consequently,

(i) Coriolis-induced vortical structures inside the inlet duct are no longer symmetric with respect to the y axis of the channel, and the higher velocities are found close to the channel bottom wall. Moreover, the rotational effects are lessened on the trailing side, with direct influence on the flow discharged close to the hub. In particular, for Ro = 0.23 and $\gamma = 45^\circ$, the

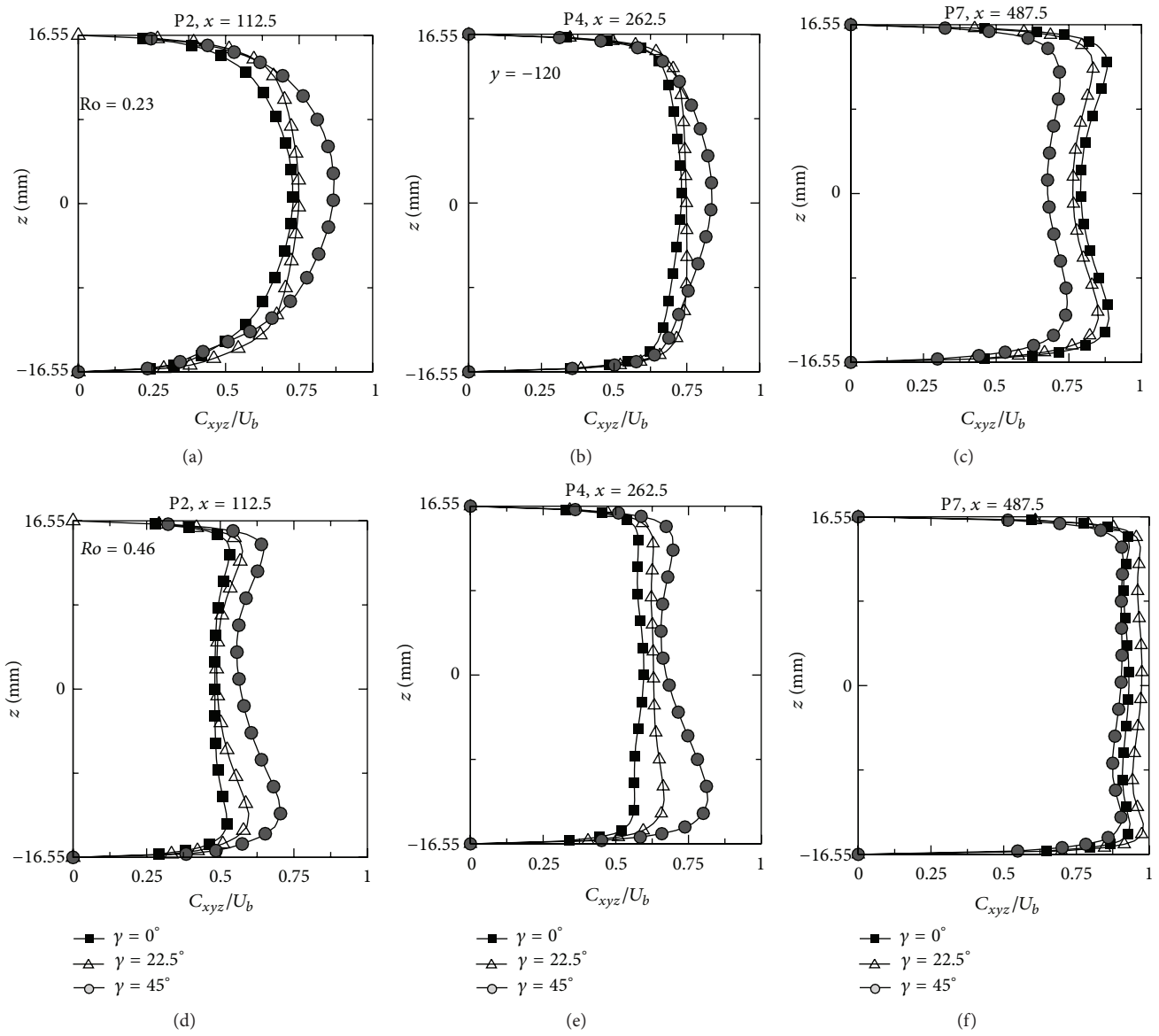

FIGURE 16: Profiles of the velocity modulus $C_{xyz} = (U^2 + V^2 + W^2)^{0.5}$ at $y = -120$ mm and different radial positions at varying γ for Ro = 0.23 (a–c) and Ro = 0.46 (d–f).

horse shoe vortices reappear on the upstream face of the first 4 pedestals.

(ii) The interaction between the asymmetric Coriolis vortices causes a flow separation all along the corner between the channel bottom and leading walls. This causes the separation bubble at the tip to have different extensions along the channel height, the larger size being found at the lowest elevations.

Nomenclature

AR: $= b/h$, Channel aspect ratio (—)
b: Channel width (m)
C_{xy}: $= (U^2 + V^2)^{0.5}$, Mean velocity modulus in plane xy (m/s)
C_{xyz}: $= (U^2+V^2+W^2)^{0.5}$, mean velocity modulus (m/s)
D_h: Hydraulic diameter (m)
h: Channel height
F_c: $= -2\rho\mathbf{\Omega}\times\mathbf{C}$, Coriolis Force per unit volume (N/m^3)
I: Turbulence intensity
r.m.s.: Root mean square value
Re: $= U_b D_h/\nu$, Reynolds number
Ro: $= \Omega D_h/U$, Rotation number
U, V, W: Mean velocity components along x, y, and z directions, respectively (m/s)
u', v', w': r.m.s. velocity fluctuations along x, y, and z directions respectively (m/s)
U_b: Bulk velocity (m/s)

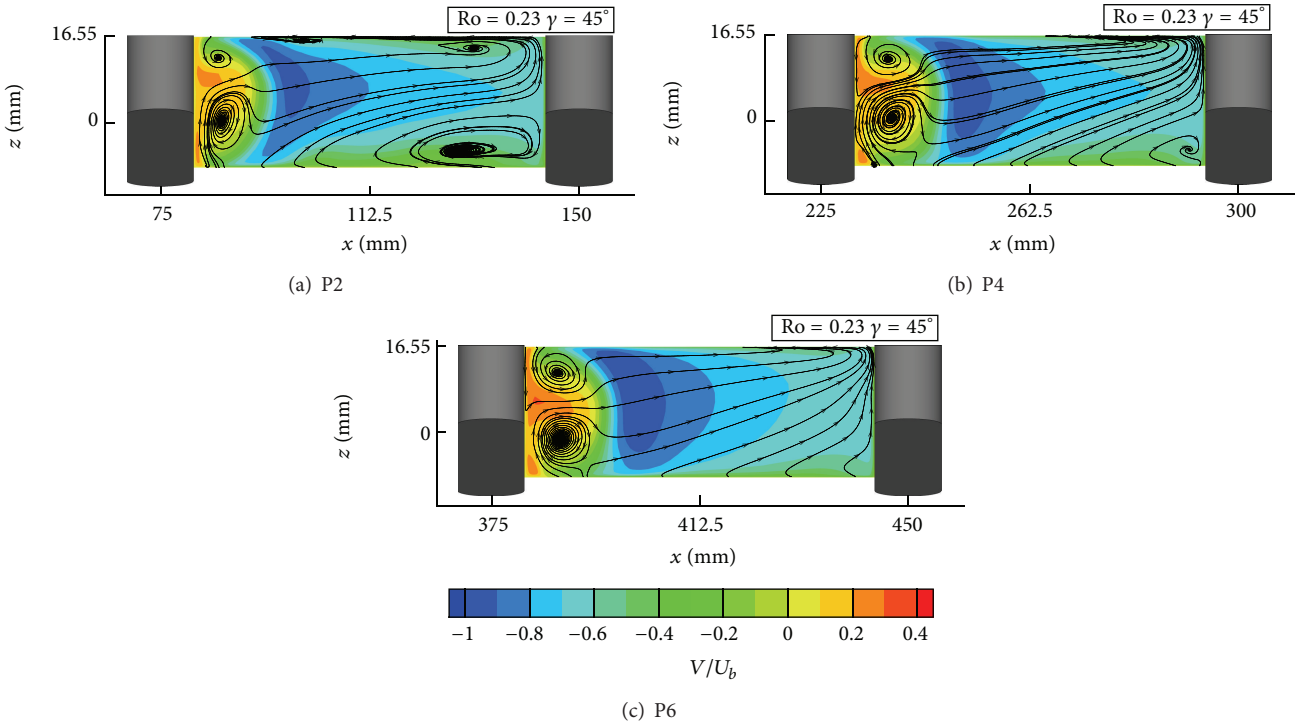

FIGURE 17: Flow field inside the interpedestal passages P2 (a), P4 (b), and P6 (c) at $y = -165$ mm for Ro = 0.23 and $\gamma = 45^{\circ}$.

X, Y, Z: Setting chamber coordinate system (mm)
x, y, z: Radial, axial, and cross wise coordinates (channel reference frame) (mm)
α: Incidence angle (deg)
ϵ: Turbulent dissipation (—)
γ: Channel orientation (deg)
κ: Turbulent kinetic energy (—)
ν: Kinematic viscosity (m^2/s)
ρ: Density (kg/m^3)
Ω: Angular velocity (rad/s).

Acknowledgment

The present work has been supported by the Italian Ministry of University and Research (MiUR).

References

[1] A. Ooi, G. Iaccarino, P. A. Durbin, and M. Behnia, "Reynolds averaged simulation of flow and heat transfer in ribbed ducts," *International Journal of Heat and Fluid Flow*, vol. 23, no. 6, pp. 750–757, 2002.

[2] M. Lohàsz, P. Rambaud, and C. Benocci, "LES simulation of ribbed square duct flow with fluent and comparison with piv data," in *Proceedings of the the 12th International Conference on Modelling Fluid Flow*, Fluid Flow Technologies, Budapest, Hungary, 2003.

[3] D. D. Luo, C. W. Leung, T. L. Chan, and W. O. Wong, "Simulation of turbulent flow and forced convection in a triangular duct with internal ribbed surfaces," *Numerical Heat Transfer A*, vol. 48, no. 5, pp. 447–459, 2005.

[4] A. K. Viswanathan and D. K. Tafti, "Detached eddy simulation of turbulent flow and heat transfer in a two-pass internal cooling duct," *International Journal of Heat and Fluid Flow*, vol. 27, no. 1, pp. 1–20, 2006.

[5] S. Spring, Y. Xing, and B. Weigand, "An experimental and numerical study of heat transfer from arrays of impinging jets with surface ribs," *Journal of Heat Transfer*, vol. 134, no. 8, Article ID 082201, 2012.

[6] R. S. Bunker, "Gas turbine heat transfer: ten remaining hot gas path challenges," *Journal of Turbomachinery*, vol. 129, no. 2, pp. 193–201, 2007.

[7] A. Armellini, F. Coletti, T. Arts, and C. Scholtes, "Aerothermal investigation of a Rib-Roughened trailing edge channel with crossing-Jets—part I: flow field analysis," *Journal of Turbomachinery*, vol. 132, no. 1, Article ID 011009, 2010.

[8] J. C. Han, "Recent studies in turbine blade cooling," *The International Journal of Rotating Machinery*, vol. 10, no. 6, pp. 443–457, 2004.

[9] J. E. Hart, "Instability and secondary motion in a rotating channel flow," *Journal of Fluid Mechanics*, vol. 45, pp. 341–351, 1970.

[10] C. G. Speziale, "Numerical study of viscous flow in rotating rectangular ducts," *Journal of Fluid Mechanics*, vol. 122, pp. 251–271, 1982.

[11] C. G. Speziale and S. Thangam, "Numerical study of secondary flows and roll-cell instabilities in rotating channel flow," *Journal of Fluid Mechanics*, vol. 130, pp. 377–395, 1983.

[12] H. Iacovides, D. Kounadis, B. E. Launder, J. Li, and Z. Xu, "Experimental study of the flow and thermal development of a row cooling jets impinging on a rotating concave surface," *Journal of Turbomachinery*, vol. 127, no. 1, pp. 222–229, 2005.

[13] M. Elfert, M. Schroll, and W. Förster, "PIV-measurement of secondary flow in a rotating two-pass cooling system with an improved sequencer technique," in *Proceedings of the ASME Turbo Expo*, pp. 555–567, Glasgow, UK, June 2010.

[14] A. K. Saha and S. Acharya, "Unsteady RANS simulation of turbulent flow and heat transfer in ribbed coolant passages of different aspect ratios," *International Journal of Heat and Mass Transfer*, vol. 48, no. 23-24, pp. 4704–4725, 2005.

[15] A. K. Saha and S. Acharya, "Turbulent heat transfer in ribbed coolant passages of different aspect ratios: parametric effects," *Journal of Heat Transfer*, vol. 129, no. 4, pp. 449–463, 2007.

[16] J. Pallares and L. Davidson, "Large-eddy simulations of turbulent flow in a rotating square duct," *Physics of Fluids*, vol. 12, no. 11, pp. 2878–2894, 2000.

[17] F. N. Felten and G. M. Laskowski, "Large eddy simulations of fully developed flow through a spanwise rotating infinite serpentine passage," in *Proceedings of the ASME Turbo Expo*, pp. 397–411, May 2007.

[18] G. M. Laskowski and P. A. Durbin, "Direct numerical simulations of turbulent flow through a stationary and rotating infinite serpentine passage," *Physics of Fluids*, vol. 19, no. 1, Article ID 015101, 2007.

[19] M. E. Taslim and T. Li, "Measurements of heat transfer coefficients in rib-roughened trailing-edge cavities with crossover jets," ASME Paper NO-98GT-435, 1998.

[20] M. E. Taslim and A. Nongsaeng, "Experimental and numerical cross-over jet impingement in an airfoil trailing-edge cooling channel," *Journal of Turbomachinery*, vol. 133, no. 4, Article ID 041009, 2011.

[21] F. Coletti, A. Armellini, T. Arts, and C. Scholtes, "Aerothermal investigation of a rib-roughened trailing edge channel with crossing jets—part II: heat transfer analysis," *Journal of Turbomachinery*, vol. 133, no. 3, Article ID 031024, 2010.

[22] F. Coletti, M. Scialanga, and T. Arts, "Experimental investigation of conjugate heat transfer in a rib-roughened trailing edge channel with crossing jets," *Journal of Turbomachinery*, vol. 134, no. 4, Article ID 041016, 2011.

[23] J.-H. Choi, S. Mhetras, J.-C. Han, S. C. Lau, and R. Rudolph, "Film cooling and heat transfer on two cutback trailing edge models with internal perforated blockages," *Journal of Heat Transfer*, vol. 130, no. 1, Article ID 012201, 2008.

[24] S. W. Chang, T.-M. Liou, S. F. Chiou, and S. F. Chang, "High rotation number heat transfer of rotating trapezoidal duct with 45-deg staggered ribs and bleeds from apical side wall," in *Proceedings of the ASME Turbo Expo*, pp. 909–921, Montreal, Canada, May 2007.

[25] Y.-H. Liu, M. Huh, L. M. Wright, and J.-C. Han, "Heat transfer in trailing edge, wedge shaped cooling channels with slot ejection under high rotation numbers," in *Proceedings of the ASME Turbo Expo*, pp. 311–320, Berlin, Germany, June 2008.

[26] A. P. Rallabandi, Y.-H. Liu, and J.-C. Han, "Heat transfer in trailing edge wedge-shaped pin-fin channels with slot ejection under high rotation numbers," in *Proceedings of the ASME Turbo Expo*, pp. 369–380, Glasgow, UK, June 2010.

[27] A. Armellini, L. Casarsa, and C. Mucignat, "Flow field analysis inside a gas turbine trailing edge cooling channel under static and rotating conditions," *International Journal of Heat and Fluid Flow*, vol. 32, no. 6, pp. 1147–1159, 2011.

[28] A. Armellini, C. Mucignat, L. Casarsa, and P. Giannattasio, "Flow field investigations in rotating facilities by means of stationary PIV systems," *Measurement Science and Technology*, vol. 23, no. 2, Article ID 025302, 2012.

[29] "ANSYS CFX-11.0 User Guide," Tech. Rep., ANSYS, 2007.

[30] I. B. Celik, U. Ghia, P. J. Roache, C. J. Freitas, H. Coleman, and P. E. Raad, "Procedure for estimation and reporting of uncertainty due to discretization in CFD applications," *Journal of Fluids Engineering*, vol. 130, no. 7, pp. 0780011–0780014, 2008.

[31] L. Richardson and A. Gaunt, "The deferred approach to the limit. Part I. single lattice. Part II. interpenetrating lattices," *Philosophical Transactions of the Royal Society of London A*, vol. 226, no. 636–646, pp. 299–361, 1927.

[32] P. J. Roache, "Perspective: a method for uniform reporting of grid refinement studies," *Journal of Fluids Engineering, Transactions of the ASME*, vol. 116, no. 3, pp. 405–413, 1994.

[33] P. J. Roache, "Conservatism of the grid convergence index in finite volume computations on steady-state fluid flow and heat transfer," *Journal of Fluids Engineering, Transactions of the ASME*, vol. 125, no. 4, pp. 731–732, 2003.